HHS Public Access

Author manuscript

Anal Chem. Author manuscript; available in PMC 2017 February 16.

Published in final edited form as:

Anal Chem. 2016 February 16; 88(4): 2015–2020. doi:10.1021/acs.analchem.5b04271.

A Frequency-domain Approach to Determine Magnetic Address-Sensor Separation Distance Using the Harmonic Ratio Method

Colin C. Young[a,c], **Benjamin W. Blackley**[†,a,c], **Marc D. Porter**[a,b,c], and **Michael C. Granger**[a,c,d,*]

[a]Department of Chemical Engineering, University of Utah

[b]Departments of Chemistry, Bioengineering, and Pathology, University of Utah

[c]Nano Institute of Utah, University of Utah, University of Utah

[d]Department of Surgery, School of Medicine, University of Utah

Abstract

In this work, we describe an approach to determine the distance separating a magnetic address from a scanning magnetoresistive sensor – a critical adjustable parameter for certain bioassay analyses where magnetic nanoparticles are used as labels. Our approach is leveraged from the harmonic ratio method (HRM), a method used in the hard drive industry to control the distance separating a magnetoresistive read head from its data platter with nanometer resolution. At the heart of the HRM is an amplitude comparison of a signal's fundamental frequency to that of its harmonics. When the signal is derived from the magnetic field pattern of a periodic array of magnetic addresses, the harmonic ratio contains the information necessary to determine the separation between the address array and the read head. The elegance of the HRM is that there is no need of additional components to the detection platform to determine a separation distance; the streaming "bit signal" contains all the information needed. In this work we demonstrate that the tenets governing HRM used in the hard drive industry can be applied to the bioanalytical arena where submicron to 100 μm separations are required.

TOC graphic

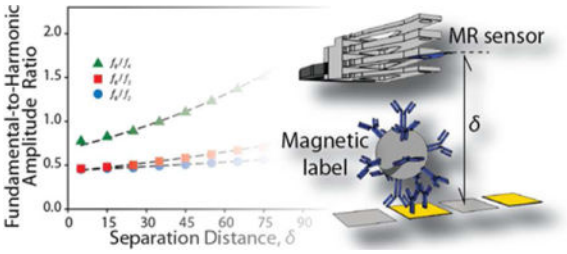

*Corresponding Author:Michael.Granger@utah.edu; (801) 587–1510; 36 S. Wasatch Dr., SMBB Rm. 5531, Salt Lake City, 84112.

†Present Addresses

Department of Mechanical Engineering, Vanderbilt University.

Introduction

Magnetoresistive (MR) sensors have emerged as an intriguing approach to detect surface bound biomarkers labeled with magnetic nanoparticles (MNPs) for bioanalytical and diagnostic purposes.[1–14] These sensors, which undergo a decrease in resistance in an externally applied field,[15] have become a mainstay in computer hard drives. The goal of translating MR sensors to the bioanalytical sciences derives from the ever continuing advances in their analytical sensitivity, speed, and compactness, all of which are important attributes of sensors destined for diagnostics, safety, and security applications.

There are two principal architectures used to take advantage of the detection capabilities of MR sensors in bioassay interrogation. The first uses the embodiment originally described by Baselt, et al.[1] in which a thin passivation layer (*e.g.*, tens of nanometers of Au or silicon nitride –Si_3N_4) deposited on the MR sensor protects it from a liquid sample.[1,7] The passivation layer also serves as a surface that can be modified with molecular recognition elements (MRE), such as antibodies or single-stranded DNA complements, to capture a target biomarker from solution. Once captured, the biomarker is selectively tagged with MNPs that have also been MRE modified. The MR sensor detects the magnetic field generated by the captured MNP, $\boldsymbol{H}_{MNP}$, which provides the means for marker quantification. However, the strength of $\boldsymbol{H}_{MNP}$ has a cubic dependence on the separation distance between sensor and MNP;[16] the closer the MNP is to the sensor the greater the signal. Assuming that the MRE and biomarker both have a thickness of 10 nm and that the MNP label is 20–100 nm in diameter, the distance between the center of the MNP label and the MR sensor, given as *d* in Figure 1, is on the order of 40–80 nm. This places the MNP in close proximity to the MR sensor.

The second architecture, which has been a focus in our laboratory,[13,14] is designed more along the lines of a hard disk drive reader. In this configuration, the assay is carried out on a sample coupon that is composed of multiple gold capture addresses interleaved with magnetic nickel reference addresses, and is physically separated from the MR sensor. The bioassay architecture is analogous to that described above where the final component is the MNP label. When the sample coupon is ready for readout it is scanned by the MR sensor.

This design differs from that originally put forth by Baselt et al. in three important ways. First, the test coupon is remote from the MR sensor, which enables the MR sensor to be used in a manner similar to that of a hard disk drive and eliminates the single use format of the earlier design. Second, future embodiments of the platform have the potential to be multiplexed with many different capture addresses for many different markers on a single, pre prepared coupon. Third, sample readout can be performed extremely rapidly by rotating the sample coupon across the sensor in air, emulating the way a computer hard drive reads magnetic data from a data platter.

The ability to detect the MNPs bound to a capture address on the test coupon hinges on minimizing the distance between the magnetic material and the MR sensor. This puts a premium on the ability to accurately control the separation distance between the sample coupon and MR sensor. Given that the magnetic field strength decays as the distance cubed,

a 10× decrease in separation distance (*e.g.*, from 10 μm to 1 μm) would theoretically increase the signal 1,000 times. However, some separation between the sensor and coupon is needed to avoid crashing the coupon into the MR surface. Typically, the physical size of the magnetic particle dictates the lower separation distance limit, which may be up to 5 μm in diameter. Therefore, a real time method to monitor and maintain a pre scribed stand-off distance is required for consistent and optimal magnetic readout.

In our previous MR based assay work, the separation distance was determined by bringing the coupon and sensor together until they were optically determined to be in contact. Once in contact, separation was achieved by manually rotating a *z*-axis lead screw. However, this method suffered from large "point of contact" estimation error, and lacked the automated control necessary for rapid, automated sample readout.

There are several methods that can be used to accurately measure the separation distances between two flat surfaces with submicron resolution, such as capacitive displacement sensors,[17–20] thin film interferometry,[20–23] and laser Doppler vibrometry,[24–26] all of which require additional components on the detection platform. However, to realize ever smaller separation distances, the hard disk industry has developed techniques to accurately determine nanometer sized separation distances between the read head and magnetic media by simply measuring the "read back" signal of the MR sensor as it is scanned across the magnetic storage medium at a constant velocity. This is advantageous, as there is no requirement for extra platform components. The approach is based on the work of Wallace and can be described by the Wallace spacing loss equation (Eq. 1).[27] Wallace showed that the amplitude of the read back signal ($A(k)_{sensor}$) decays exponentially in the frequency domain as the separation distance between the MR transducer and the magnetic media increases,[28] specifically:

$$A(k)_{sensor} = S_{sensor} J_{medium} e^{-kd} \quad \text{Eq. 1}$$

where S_{sensor} is the sensitivity of the magnetic transducer, J_{medium} describes the magnetic properties of the medium, and d is the separation distance between transducer and medium. The spatial frequency, k, is defined as $k = 2\pi/\lambda = 2\pi f/v$, where λ is the signal wavelength (*i.e.*, the distance between two magnetic addresses or bits), f is the signal frequency, and v is the translation velocity of the transducer or medium with respect to each other (*i.e.*, scan speed). As evident in Eq. 1, the signal amplitude in the frequency domain decreases exponentially as either d increases or λ decreases.

Several approaches, based on different forms of the Wallace spacing loss equation, have been developed and used to determine d, including the pulse width half max,[29] read back signal modulation,[30] and harmonic ratio methods (HRM).[31–33] The advantages of the HRM over the other two methods are its independence of read head and media type (*i.e.*, parallel or longitudinal magnetic media), and it can be used if the magnetization pattern unexpectedly changes, as long as it remains constant during the measurement.[32] Moreover, by using a ratio approach (see below), factors that may affect signal amplitude (*e.g.*, amplifier gain or head efficiency) are canceled out as they affect the harmonic amplitudes in exactly the same way. The HRM does, however, require that:[34] the read head have a linear

response over the range of measured signal amplitudes; the magnetic configuration should be two dimensional; the reader width or address width should be considerably wider than $\lambda/2\pi$; and the vertical field component should be measured to maintain fidelity with the Wallace predictions.

In the HRM approach, the sampled read back signal of a periodic, magnetic signature is converted to the frequency domain by use of the Fast Fourier Transform. The resulting fun damental frequency (f_0) and harmonic frequencies (f_i, i = 2, 3 etc.), each of which is an integer multiple of the fundamental frequency, are analyzed as the amplitude ratio of the fundamental to that of a given harmonic. An example of an amplitude ratio between the fundamental ($k_0 = 2\pi/\lambda$) and the third harmonic ($k_3 = 6\pi/\lambda = 3k_0$) is given in Eq. 2.

$$\frac{A(k_0)}{A(k_3)} = S_{k_0/k_3} J_{k_0/k_3} \frac{e^{-k_0 d}}{e^{-3k_0 d}} = S_{k_0/k_3} J_{k_0/k_3} e^{2k_0 d} \quad \text{Eq. 2}$$

Inspection of Eq. 2 indicates that each amplitude ratio can be described by a unique analytical expression in which the *y*-intercept and slope are adjustable. The utility of this approach is well proven in hard drive applications where the magnetic media is contiguous and magnetic field transitions (*i.e.*, data bits) occur over a finite length.

In this paper, we explore the extensibility of the HRM as a means to determine the separation distance between an MR sensor and a sample coupon, which is patterned with a one-dimensional array of alternating gold and magnetic nickel addresses. During the course of MR based bioassays, the gold addresses are used for analyte capture and the nickel addresses serve as c ex periments, only four nickel addresses are used. The experiments were performed by scanning an MR sensor across the four nickel addresses. The read back signal was then analyzed in the frequency domain to determine amplitude ratios at separation distances ranging from 105 to 5 μm. These amplitude ratios were fit to a two parameter exponential equation, and compared to the results from a finite difference model of the sample coupon. Using this method, we were able to determine the separation distance between the sample coupon and MR sensor between 5 and 105 μm with submicron resolution. While validated in our specific application, we expect the HRM can be extended to any number of applications as a technique to determine absolute separation distances.

Experimental Section

A schematic of the test coupon immersed in $\boldsymbol{H}_{app}$ (100 Oe) and the MR sensor are shown in Figure 1. (Preparation of the test coupons has been previously described,[7,13,14] and details are given in the Supporting Information.). A chromatic confocal imaging optical probe[35] was used to verify the separation distance between the test coupon and MR sensor and to calibrate our *z*-axis stepper motor. Note that $\boldsymbol{H}_{app}$ and the scan direction are aligned with the *x*-axis of the coupon.

The 200×200 μm MR sensor[36] (see Supporting Information) was translated across the test coupon as a function of separation between the test coupon and the MR sensor (*z*-axis) and data were acquired at 5.8 Hz. The resulting signal at each separation distance was

transformed to the frequency domain using the Fast Fourier Transform (FFT) to determine the amplitudes of the resulting fundamental and harmonic frequencies. These data were compared to that predicted by a finite-element two dimensional model.

Results and Discussion

Sample Coupon Scans

Four nickel addresses on a single test coupon were aligned directly over the MR sensor and scanned at a velocity of 31.1 μm/s relative to the stationary coupon at separations ranging from 5 to 105 μm in 10 μm increments. A subset of the resulting response is shown in Figure 2A at separation distances of 5, 55, and 105 μm. The signal transient across each address exhibits the same characteristic shape composed of a minimum – the center of each nickel address – surrounded by two smaller maxima – the leading and trailing edges of the nickel addresses (the evolution of the magnetic transient has been previously described[14]). Between each address, the signal re turns to the baseline voltage observed when the sensor is located beyond the magnetic field of the nickel addresses. As the separation distance decreases, the magnitudes of the maxima and minima features increase due to an increased flux density from the nickel addresses detected by the MR sensor. The trailing edge maxima features are slightly larger than the leading edge feature, which is likely due to a slight misalignment of the addresses as they are scanned across the MR sensor.

Shown in Figure 2B are the FFT results of the signal trans formation. The frequency spectra contain five frequencies, *viz.* the fundamental frequency (f_0) at 22.2±0.1 mHz, and harmonic frequencies of $f_2 = 2f_0 = 44.4\pm0.1$ mHz; $f_3 = 66.7\pm0.1$ mHz; $f_4 = 88.9\pm0.1$ mHz; and $f_5 = 111.1\pm0.1$ mHz. The fundamental frequency matches the expected frequency from the read ve locity (*i.e.*, a scan rate of 31.1 μm/s and spatial wavelength of 1,400 μm). As the separation distance decreases, the amplitudes of the fundamental and harmonics increase at different rates, validating the utility of the HRM for our system.

Amplitude ratios were determined at each separation distance for the fundamental divided by the 2nd (f_0/f_2), 3rd (f_0/f_3), and 4th (f_0/f_4); the 5th harmonic was excluded due to the weak signal at large separation distances. Using a non linear least squares regression, each quotient as a function of separation distance was fit to a two parameter exponential, $y=Qe^{bd}$, a reduced version of Equation 2, with Q and b as fitting parameters. The resulting fits are shown in Figure 3 and the two fitting parameters are summarized in Table 1; the error for each fit is calculated at the 95% confidence level.

According to the reduced version of Eq. 2, the estimated b parameter should be a function of the signal wavelength. However, all of the calculated wavelengths ($\lambda = 2\pi/b$ for f_0/f_2, $4\pi/b$ for f_0/f_3, and $6\pi/b$ for f_0/f_4) tabulated in Table 1 overestimate the signal wavelength, but appear to be converging toward the true wavelength of 1,400 μm at higher order harmonic quotients. The calculated values of Q represent the product of sensor sensitivity, S, and nickel address magnetic proper ties, J, as a function of harmonic quotient. This value is the sensor response as a function of harmonic ratio when d equals zero, *i.e.*, the y intercept. These analytical expressions can be used as empirical relations to determine separation distances down to the 1–5 μm range that we require in our system. We speculate that the

deviation from the HRM prediction is partially a result of the millihertz frequencies used in these experiments and partially due to the width of sensor and addresses being identical.[32]

The usefulness of each quotient, *i.e.*, its slope – the sensitivity – depends upon the separation distance. At small separation distances where higher order harmonics have large amplitudes, f_0/f_4 is more analytically useful than the lower order harmonics. As the separation distance increases, the higher harmonic amplitudes become indistinguishable from the noise, the slope becomes infinite and it is no longer useful. However, at these larger separation distances the lower order harmonic ratios can still be used, giving the system a large dynamic range.

Modeling

A two dimensional model was created of four nickel addresses in a layout that matched that of the sample coupon (see Supporting Information). A field of 100 Oe was applied in the *x*-direction (down the length of the coupon) and the induced field from the nickel addresses as a function of position was calculated at separation distances of 5 to 105 μm in 10 μm increments, in order to match the experimental setup. Since the MR sensor is finite (200×200 μm) and not a point sensor, the magnetic field data from the model was integrated over a 200 μm segment in the *x*-direction. This segment was then moved forward in 1 μm increments with the integration per formed at each increment. The integrated field was converted from position to time assuming a scan velocity of 31.1 μm/s.

The shape of the integrated magnetic field at separation distances of 5, 55, and 105 μm agrees with that observed experimentally (see Figure SI–1A). The predicted magnitude of the signal is larger than that observed experimentally, which will be discussed shortly. The magnitudes of the signal features increase as the separation distance decreases, which indicates that the frequency spectrum of the signal should have a dependence on separation distance.

Observed after transformation to the frequency domain (see Figure SI–1B) is a fundamental frequency (f_0) at 22.2 mHz and five harmonics, which are each an integer multiple of the fundamental frequency (f_2 at 44.4 mHz, f_3 at 66.7 mHz, f_4 at 88.9 mHz, f_5 at 111.1 mHz, and f_6 at 133.2 mHz). This is in agreement with the frequencies from our experimental data, though the modeling predicts the presence of a 6^{th} harmonic which was not observed in our experimental data. The amplitudes of the fundamental and harmonic frequencies increase at different rates as the separation distance decreases, which match the trends of the experimental data.

Within error, a plot of the amplitude ratio fits for the 2^{nd}, 3^{rd} and 4^{th} harmonics (see Figure SI–2A) yield the same values for the *b* parameter as determined from the experimental data ($b_1 = 0.0031$, $b_2 = 0.0071$, $b_3 = 0.0114$) and thus the same predicted wavelengths. This indicates that the *b* parameter is fun damentally dependent on the signal wavelength as predicted from theory. As a result, the model is an effective method to qualitatively predict the impact of different coupon configurations and scan speeds that will be used as we continue to optimize the performance of our system.

Interestingly, the harmonic amplitudes are larger and the resulting ratios are smaller than those observed experimentally, which seems to imply that the experimental data was collected at a distance much greater than indicated in the modeling. We attribute this to a combination of factors stemming from the 2D model of a 200 μm sensor not matching the 3D physical situation of our Wheatstone bridge MR sensor configuration. Also the matched size of the sense pad and nickel address, *i.e.*, 200×200 μm, may result in a loss of field resolution that would result in broadening of the signal features, and an apparent increase in separation distance in the harmonic analysis.

The model and experimental data can be brought into strong agreement, however, if the model data is evaluated using an effective distance. If we define an effective distance parameter, *c*, and add it to the exponential fits, as shown in Equation 3, we can estimate an effective distance that can be used to bring the theory and data closer into agreement.

$$\frac{A(k_0)}{A(k_3)} = S_{k_0/k_3} J_{k_0/k_3} e^{2k_0(d+c)} \quad \text{Eq. 3}$$

When the model amplitude ratio fit equations are evaluated at a distance of *d*+95 μm, the exponential fits are nearly equivalent to the experimental data (see Figure SI–2B).

Through the use of the model, we have validated our experimental results and developed a method to predict how the amplitude ratios will change as a function of separation distance and spacing between the nickel addresses on the sample coupons. By using an effective distance parameter of *c* = 95 μm, we believe that we will be able to accurately predict the amplitude ratios for different sample coupon configurations. Modeling also predicts that at even smaller separation distances – less than one micron – the utility of the f_0/f_5 and f_0/f_6 ratios will become apparent as their analytical sensitivities are predicted to be much greater than the lower order harmonic ratios at these distances. When sample architecture and labeling strategy permit, readout at submicron separation distances will improve our measurement resolution and improve limits of detection. Going forward, the model will be used to inform design decisions as we continue to develop our MR sensor platform for bioanalytical use.

Conclusions

Through this work, we have determined the HRM to be an effective method for determining separation distances between 5 μm and 105 μm for our MR biosensor platform. Using this method, we can achieve a prescribed separation between an MR sensor and sample coupon with submicron resolution. By transforming the signal to the frequency domain and monitoring the amplitude ratios of the fundamental frequency to a series of harmonics, we expect to be able to determine the separation distance with micron resolution and in near real time as we scan our sample coupons. From the data, it appears that this method can be extended over a large dynamic range, since the analytical sensitivity of a particular ratio differs de pending on the separation distance range of interest.

Also, we developed a finite difference model that can be used to help inform future platform development. From the model data, the wavelength dependence of the exponential factor, *b*,

found experimentally was confirmed by theory. The amplitude ratio fit equations from the model data matched the empirical data when evaluated at an effective distance of d+95 μm, which is likely due to the non idealities of the 2D model when compared to the physical system. The frequency spectrum from the model data also suggested the presence of a 6^{th} harmonic that we expect will be seen as the separation distance is decreased below a micron.

The HRM is an effective technique for determining the separation distance between two surfaces in relative motion and can potentially be applied to many systems, not just the MNP/MR based bioassay we show here. By either patterning a periodic magnetic signal or monitoring an inherent, periodic magnetic signal, separation distance can be accurately determined through the transformation of the read back signal and monitoring of the subsequent frequency content of the signal.

The HRM will be used in future embodiments of our MR biosensor platform in which a multiplexed sample coupon is rapidly rotated relative to the sensor for readout. By maintaining the interleaved pattern of nickel internal reference ad dresses and gold capture addresses on a sample coupon, the separation distance can be continually measured and controlled to maintain signal strength and fidelity. This translates to a larger magnetic signal to noise ratio and superior limits of detection than current designs. This rapid, multiplexed plat form has significant diagnostic and medical surveillance implications.

Supplementary Material

Refer to Web version on PubMed Central for supplementary material.

Acknowledgments

This work was supported by the National Institutes of Health (U01CA151650) and the Utah Science Technology and Research (USTAR) Initiative. CCY acknowledges support from the National Science Foundation Graduate Research Fellowship Program (Grant Number 1256065). CCY and BWB acknowledge support from the National Science Foundation Integrative Gradu ate Education and Research Traineeship (IGERT DGE 0903715).

References

1. Baselt DR, Lee GU, Natesan M, Metzger SW, Sheehan PE, Colton RJ. Biosens Bioelectron. 1998; 13:731–739. [PubMed: 9828367]
2. Edelstein RL, Tamanaha CR, Sheehan PE, Miller MM, Baselt DR, Whitman LJ, Colton RJ. Biosens Bioelectron. 2000; 14:805–813. [PubMed: 10945455]
3. Schotter J, Kamp PB, Becker A, Puehler A, Brinkmann D, Schepper W, Brueckl H, Reiss G. IEEE Trans Magn. 2002; 38:3365–3367.
4. Graham DL, Ferreira HA, Freitas PP, Cabral JMS. Biosens Bioelectron. 2003; 18:483–488. [PubMed: 12604266]
5. Li G, Joshi V, White RL, Wang SX, Kemp JT, Webb C, Davis RW, Sun S. J Appl Phys. 2003; 93:7557–7559.
6. Ferreira HA, Graham DL, Feliciano N, Clarke LA, Amaral MD, Freitas PP. IEEE Trans Magn. 2005; 41:4140–4142.
7. Millen RL, Kawaguchi T, Granger MC, Porter MD, Tondra M. Anal Chem. 2005; 77:6581–6587. [PubMed: 16223243]
8. Han SJ, Xu L, Yu H, Wilson RJ, White RL, Pourmand N, Wang SX. Technical Digest, International Electron Devices Meeting. 2006; 1:451–454.

9. de Boer BM, Kahlman JAHM, Jansen TPGH, Duric H, Veen J. Biosens Bioelectron. 2007; 22:2366–2370. [PubMed: 17084072]
10. Wang SX, Li G. IEEE Trans Magn. 2008; 44:1687–1702.
11. Srinivasan B, Li Y, Jing Y, Xing C, Slanton J, Wang JP. Anal Chem. 2011; 83:2996–3002. [PubMed: 21417448]
12. Rizzi G, Osterberg FW, Dufva M, Hansen MF. Biosens Bioelectron. 2014; 52:445–451. [PubMed: 24094523]
13. Millen RL, Nordling J, Bullen HA, Porter MD, Tondra M, Granger MC. Anal Chem. 2008; 80:7940–7946. [PubMed: 18826241]
14. Nordling J, Millen RL, Bullen H, Porter MD, Tondra M, Granger MC. Anal Chem. 2008; 80:7930–7939. [PubMed: 18826239]
15. Baibich M, Broto J, Fert A, Van Dau F, Petroff F, Etienne P, Creuzet G, Friederich A, Chazelas J. Phys Rev Lett. 1988; 61:2472–2475. [PubMed: 10039127]
16. Cullity, BD.; Graham, CD. Introduction to Magnetic Materials. 2nd. John Wiley & Sons Inc; Hoboken, New Jersey: 2009. p. 543
17. Briggs GR, Herkart PG. IEEE Trans Magn. 1971; 7:418–421.
18. Bonse M, Zhu F, Van Beek H. Meas Sci Technol. 1993; 4:801.
19. Kim M, Moon W, Yoon E, Lee K-R. Sens Actuators, A. 2006; 130:135–141.
20. Lin C. IEEE Trans Magn. 1973; 9:673–677.
21. Fleischer JM, Lin C. IBM Journal of Research and development. 1974; 18:529–533.
22. Nigam A. J Tribol. 1982; 104:60–65.
23. Lin C, Sullivan R. IBM Journal of Research and Development. 1972; 16:269–276.
24. Castellini P, Martarelli M, Tomasini E. Mechanical Systems and Signal Processing. 2006; 20:1265–1285.
25. Roos P, Stephens M, Wieman C. Appl Opt. 1996; 35:6754–6761. [PubMed: 21151259]
26. Johansmann M, Siegmund G, Pineda M. Proc IDEMA. 2005:1–12.
27. Wallace R. Bell System Technical Journal. 1951; 30:1145–1173.
28. Dietzel A, Berger R, Machtle P, Despont M, Haberle W, Stutz R, Binnig GK, Vettiger P. Sens Actuators, A. 2002; 100:123–130.
29. Klaassen KB, Peppen JCLv. IEEE Trans Instrum Meas. 1994; 43:121–127.
30. Shi WK, Zhu LY, Bogy DB. IEEE Trans Magn. 1987; 23:233–240.
31. US Patent Number. 4,777,544. 1988.
32. Klaassen KB, van Peppen JC. IEEE Trans Magn. 2001; 37:575–582.
33. Yuan ZM, Liu B. IEEE Trans Magn. 2006; 42:341–343.
34. Marchon B, Saito K, Wilson B, Wood R. IEEE Trans Magn. 2011; 47:3422–3425.
35. Browne MA, Akinyemi O, Boyde A. Scanning. 1992; 14:145–153.
36. Rife JC, Miller MM, Sheehan PE, Tamanaha CR, Tondra M, Whitman LJ. Sens Actuators, A. 2003; A107:209–218.

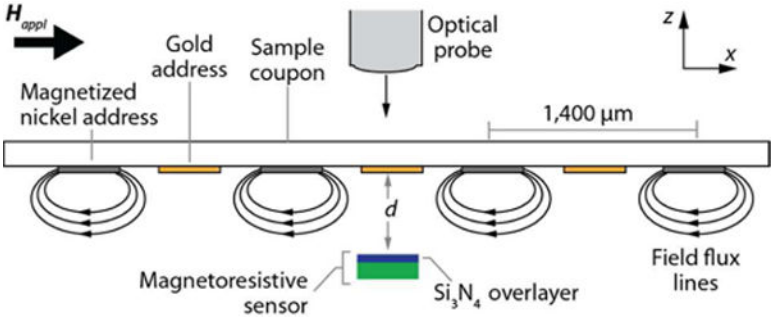

Figure 1.

A diagram of a portion of a sample coupon, MR sensor, and optical probe. Four nickel addresses, in the presence of an applied field (***H*****$_{app}$**), are scanned over an MR sensor at various separation distances (***d***). The figure is not drawn to scale.

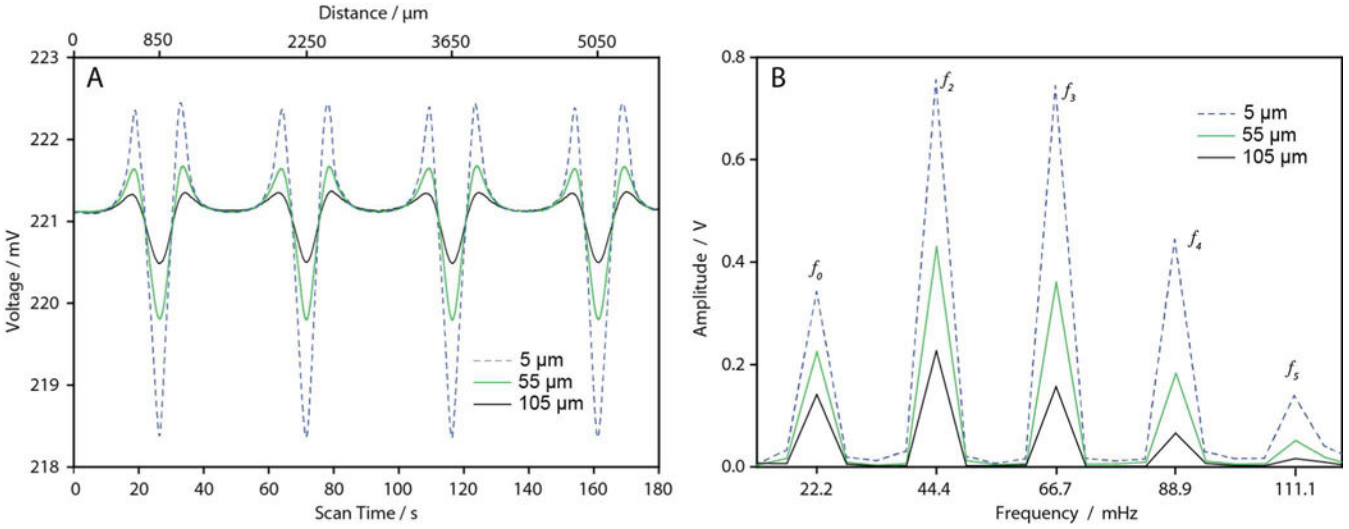

Figure 2.

(**A**) Voltage recorded from four nickel addresses during scans with the MR sensor at different separation distances (5 µm, blue; 55 µm, red; and 105 µm, black). As the separation distance decreases, the magnitude of the signal features increases due to an increased magnetic flux detected by the sensor. (**B**) Frequency spectrum of MR response contains a fundamental frequency (f_0) at 22.2±0.1 mHz and four harmonics (f_2 at 44.4±0.1 mHz, f_3 at 66.7±0.1 mHz, f_4 at 88.9±0.1 mHz, and f_5 at 111.1±0.1 mHz).

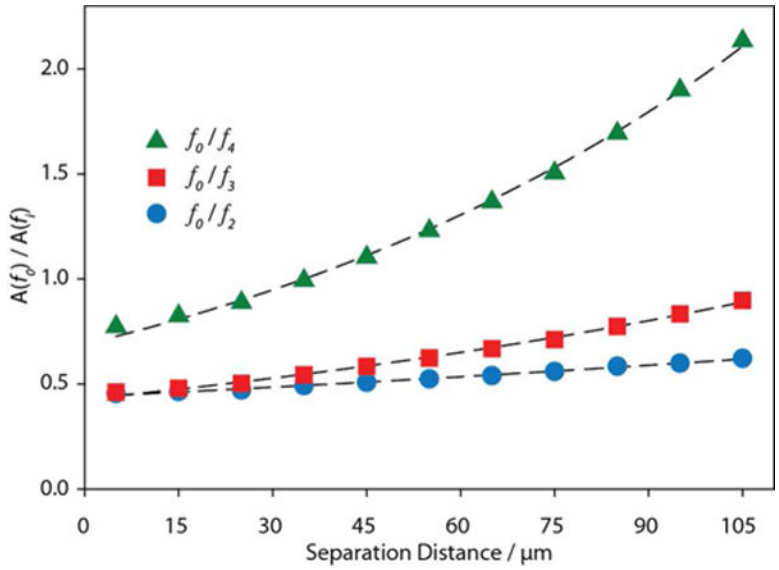

Figure 3.

Plot of the harmonic ratios as a function of separation distance. The amplitude (*A)* ratios of the fundamental frequency to the 2nd (circles), 3rd (squares), and 4th (triangles) harmonics are shown at each separation distance. The dashed lines represent the best fit lines, as determined through least squares fitting of the data to a two parameter exponential expression. Errors bars are smaller than the data points, and are a result of the 10 μV noise in the signal. The 5th harmonic was excluded due to the weakness of the signal at the larger separation distances.

Table 1

Calculated Fit Parameters for Harmonic Ratios.

	Q	b (μm^{-1})	λ_{pred} (μm)	R^2
f_0/f_2	0.439±0.005	0.0033±0.001	1,920	0.995
f_0/f_3	0.428±0.009	0.0070±0.001	1,800	0.997
f_0/f_4	0.689±0.020	0.0106±0.001	1,770	0.998